Geophysical Journal International

Geophys. J. Int. (2022) **230,** 908–915 https://doi.org/10.1093/gji/ggac099
GJI Seismology

Transient poroelastic response to megathrust earthquakes: a look at the 2015 M_w 8.3 Illapel, Chile, event

Haozhe Yang [1,2] Rumeng Guo,[1] Jiangcun Zhou,[1] Hongfeng Yang [3] and Heping Sun[1]

[1]*State Key Laboratory of Geodesy and Earth's Dynamics, Innovation Academy for Precision Measurement Science and Technology, Chinese Academy of Sciences, Wuhan* 430077*, China. E-mail: guorm@asch.whigg.ac.cn*
[2]*College of Earth and Planetary Sciences, University of Chinese Academy of Sciences, Beijing* 100049*, China*
[3]*Earth System Science Programme, The Chinese University of Hong Kong, Shatin, Hong Kong,* 999077*, China*

Accepted 2022 March 7. Received 2022 February 16; in original form 2021 June 22

SUMMARY

Large earthquakes can alter regional groundwater pressure, resulting in fluid flow, and the process of restoring hydrostatic equilibrium would in turn lead to observable surface deformation, termed poroelastic rebound, which is one of the most important post-seismic mechanisms for stress transfer and triggering. To constrain the poroelastic contributions to the early post-seismic deformation, we model the hydrologic response within 1.5 months following the 2015 M_w 8.3 Illapel earthquake and remove its effects from the observed geodetic signals. Results demonstrate the post-seismic fluid-flow patterns from the co-seismic high-slip region to the north and south sides, and the northern poroelastic effects are remarkably stronger than those on the south side, verified by northern liquefaction phenomena. Therefore, previous pure afterslip models overestimate the asperities on both flanks of the co-seismic rupture zone and underestimate the middle region, with local errors of more than 50 per cent. It highlights the importance of considering the poroelastic effects, when modelling the transient post-seismic deformation.

Key words: High-pressure behaviour; Permeability and porosity; Satellite geodesy; Earthquake ground motions.

1 INTRODUCTION

After large earthquakes, crustal deformation is accommodated by multiple post-seismic processes with different temporal and spatial scales, such as afterslip, poroelastic rebound, and viscoelastic relaxation or fault relocking (e.g. Bürgmann & Dresen 2008; Freed *et al.* 2017). Although co-seismic ruptures release the accumulated strain on the fault plane, they could increase stresses in the surrounding regions. These stresses may be transmitted to the velocity-strengthening regions on the fault, causing afterslip (e.g. Marone *et al.* 1991). They could also alter the pore pressure gradients in the surrounding rock, leading to fluid flow in the crust and gradually returning to the hydrostatic equilibrium, termed poroelastic rebound (e.g. Peltzer *et al.* 1996). Besides, ductile lower crust and mantle may relax and flow due to 'viscoelastic relaxation', which gradually transfers these stresses to the elastic upper crust, resulting in a wider range of stress increases (e.g. Freed & Lin 2001; Guo *et al.* 2019a). The combined effects of these different mechanisms produce surface deformation that was observed through geodetic measurements (Malservisi *et al.* 2015). However, distinguishing the contribution from different post-seismic mechanisms is difficult because of the similarities in their induced deformation.

When geodetic observations are used to decipher post-seismic mechanisms, viscoelasticity is considered to be only important for the long-term deformation (e.g. Shrivastava *et al.* 2016; Huang *et al.* 2017; Klein *et al.* 2017; Guo *et al.* 2019b). For transient post-seismic deformation, it is commonly assumed that afterslip plays the dominant role, and the effects of poroelasticity are ignored (e.g. Shrivastava *et al.* 2016; Freed *et al.* 2017; Huang *et al.* 2017; Guo *et al.* 2019a). However, poroelastic relaxation caused by shallow subsurface fluid plays an important role in the early post-seismic deformation (McCormack & Hesse 2018; McCormack *et al.* 2020). It is usually thought to occur within a few days or weeks after an earthquake and is concentrated in the crust (Perfettini & Avouac 2004; Barbot *et al.* 2009; Freed *et al.* 2017), yet little is known about its specific spatial and temporal distribution.

The near-field post-seismic transients in pore pressure, fluid flux and surface deformation, consistent with poroelastic behaviour, have been observed widely (Peltzer *et al.* 1996; Jonsson *et al.* 2003), which are conducive to simulate the poroelastic deformation. McCormack *et al.* (2020) analysed the post-seismic mechanisms during the first 40 d following the 2012 M_w 7.6 Nicoya earthquake and suggested that a pure afterslip model ignoring the poroelastic effects may introduce errors up to 50 per cent. By investigating the 2-yr

fluid-related process of the 2011 M_w 9.0 Tohoku earthquake, Hu *et al.* (2014) found that the poroelastic rebound produced surface displacements up to dozens of centimetres in both horizontal and vertical components, promoting a better interpretation of the heterogeneity of post-seismic deformation following large subduction zone earthquakes. Therefore, separating the poroelastic components and afterslip in the post-seismic deformation is helpful to better understand the characteristics of post-seismic mechanisms, which is of great significance for early post-seismic hazard assessment, as they were often accompanied by repeated earthquakes and aftershock swarms (Poli *et al.* 2017).

Here, we focus on modelling the poroelastic effects in the post-seismic phase of subduction zone earthquakes, with application in the 2015 M_w 8.3 Illapel earthquake. This event struck central Chile along the megathrust interface between the Nazca Plate and the South American Plate, where the Nazca Plate is subducting beneath the South American Plate with a rapid convergence rate of $\sim$66 mm yr^{-1}, resulting in frequent earthquakes (e.g. Angermann *et al.* 1999). Co-seismic rupture characteristics have been characterized by different data and methods (e.g. Barnhart *et al.* 2016; Shrivastava *et al.* 2016; Tilmann *et al.* 2016; Yin *et al.* 2016; Klein *et al.* 2017; Guo *et al.* 2019a). Several studies used GPS (global positioning system)/InSAR data to explore the early post-seismic deformation, mostly relying on pure elastic afterslip models (Shrivastava *et al.* 2016; Huang *et al.* 2017; Klein *et al.* 2017). However, obvious liquefaction phenomena have been reported near two GPS stations, BTON and LSCH, in the northern source region after the Illapel earthquake (Gregory *et al.* 2015; Candia *et al.* 2017). Candia *et al.* (2017) suggested that the post-seismic reconnaissance is polluted by the tsunami, indicating that the actual occurrence of liquefaction may be more widespread. In addition, Poli *et al.* (2017) outlined three areas with high pore fluid pressure in the Illapel seismic area based on the geological interpretation of the magnetic intensity anomaly, the free-air gravity anomaly, the swath bathymetric data and aftershock distribution (Fig. 1). These observations reveal that fluids may play an important role in the transient post-seismic process. Fortunately, there is a continuous GPS (cGPS) observation network with good azimuth around the source region, providing an unprecedented opportunity for us to unravel the regional post-seismic pore fluid effects. Herein, we probe the 1.5-month post-seismic deformation following the 2015 Illapel earthquake by using the pure afterslip model and the combined model involving poroelastic effects.

2 DATA AND METHODS

We collect the post-seismic displacements of 13 permanent cGPS stations from the work of Shrivastava *et al.* (2016). In this work, we systematically investigate the physical mechanisms of early post-seismic deformation after the Illapel earthquake. Specifically, we construct two different models: (i) pure afterslip only and (ii) the combined model of afterslip and poroelasticity. All make use of an inversion routine to minimize the discrepancies between the model predictions and data observations. In the following, we will briefly introduce the theories and methods. Given that the observed horizontal displacements are consistent in sense to the co-seismic surface deformation, indicating afterslip indeed makes great contributions to the transient post-seismic deformation (Barnhart *et al.* 2016; Shrivastava *et al.* 2016), so herein we do not consider the individual poroelastic model.

2.1 Pure afterslip model

Afterslip is generally confined within velocity-strengthening regions, updip or downdip of the rupture zone (e.g. Marone *et al.* 1991; Guo *et al.* 2019b). Afterslip mainly controls the near-field deformation and can last for several months or even years, which plays a crucial role in deciphering fault friction behaviours (Helmstetter & Shaw 2009). In our work, the steepest descent method, a high-efficiency gradient method (Wang *et al.* 2009; Guo *et al.* 2019b; Tang *et al.* 2021), is used to derive the afterslip distribution. To obtain the high-resolution slip distribution, the fault plane is usually discretized into many rectangular or triangle subfaults. When the fault geometry is fixed, the relationship between surface observations and fault slip can be written as

$$\mathbf{y} = \mathbf{Gm} + \varepsilon, \tag{1}$$

where $\mathbf{G}$ is the Green's function, which can be calculated by the dislocation theory in elastic half-space or layered earth model; $\mathbf{m}$ represents the slip vector of the subfaults, including the components of strike and dip; ε indicates the errors, which are composed of the observation errors and theoretical errors caused by model simplification; and $\mathbf{y}$ represents the surface deformation. To obtain stable and reliable results, prior constraints should be introduced. Bouchon (1997) proposed that the stress drop is positively correlated with the slip magnitude, meaning high slip occurs in areas with large stress drop. To restrict slip models to those with an appropriate stress drop distribution or slip roughness, we define the objective function by (Wang *et al.* 2009)

$$F(\mathbf{m}) = \|\mathbf{Gm} - \mathbf{y}\|^2 + \beta^2 \|\mathbf{H}\tau\|^2. \tag{2}$$

Here, $\mathbf{H}$ represents the product of the finite-difference approximation of the Laplace operator and the weighted factor of slip amplitude; τ indicates the stress drop associated with slip; and β is the smoothing factor, which could be determined by a trade-off between model roughness and data misfit.

2.2 Combined model

To construct a combined model of afterslip and poroelasticity, we first need to estimate the poroelastic effects. Some studies evaluated the post-seismic poroelastic effects by the difference between two co-seismic solutions based on the drained and undrained Poisson's ratio (e.g. Peltzer *et al.* 1996; Jonsson *et al.* 2003; Wang *et al.* 2019), but the complexity is missed and uncertainties are great (McCormack *et al.* 2020). Given that the poroelastic effects related to the local geological structure are complex and elusive (Roeloffs 1996; Cheng 2016), it is difficult to carry out inversion directly. We thus use forward modelling to analyse the surface deformation caused by poroelastic relaxation. In this work, we adopt the linear poroelastic theory (Biot 1941), which describes the coupling of pore fluid flow and rock deformation (Biot 1941; Wang 2000; Wang & Kumpel 2003; McCormack *et al.* 2020):

$$(\lambda + 2\mu)\nabla(\nabla \cdot \mathbf{u}) - \mu\nabla \times (\nabla \times \mathbf{u}) - \alpha\nabla p = \mathbf{f}(\mathbf{x}, t) \tag{3}$$

$$Q^{-1}\frac{\partial p}{\partial t} + \alpha\frac{\partial}{\partial t}\nabla \cdot \mathbf{u} - \chi\nabla^2 p = q(\mathbf{x}, t), \tag{4}$$

where $\mathbf{u}$ represents the displacement vector; λ and μ are the Lamé parameters; p is the pore pressure; and $\mathbf{f}$ is the force per unit volume acting on the solid matrix, which is the function of time t and spatial position $\mathbf{x}$. The parameter q is the fluid volume injection rate, which is set as 0 here; α indicates the Biot–Willis parameter; χ is the

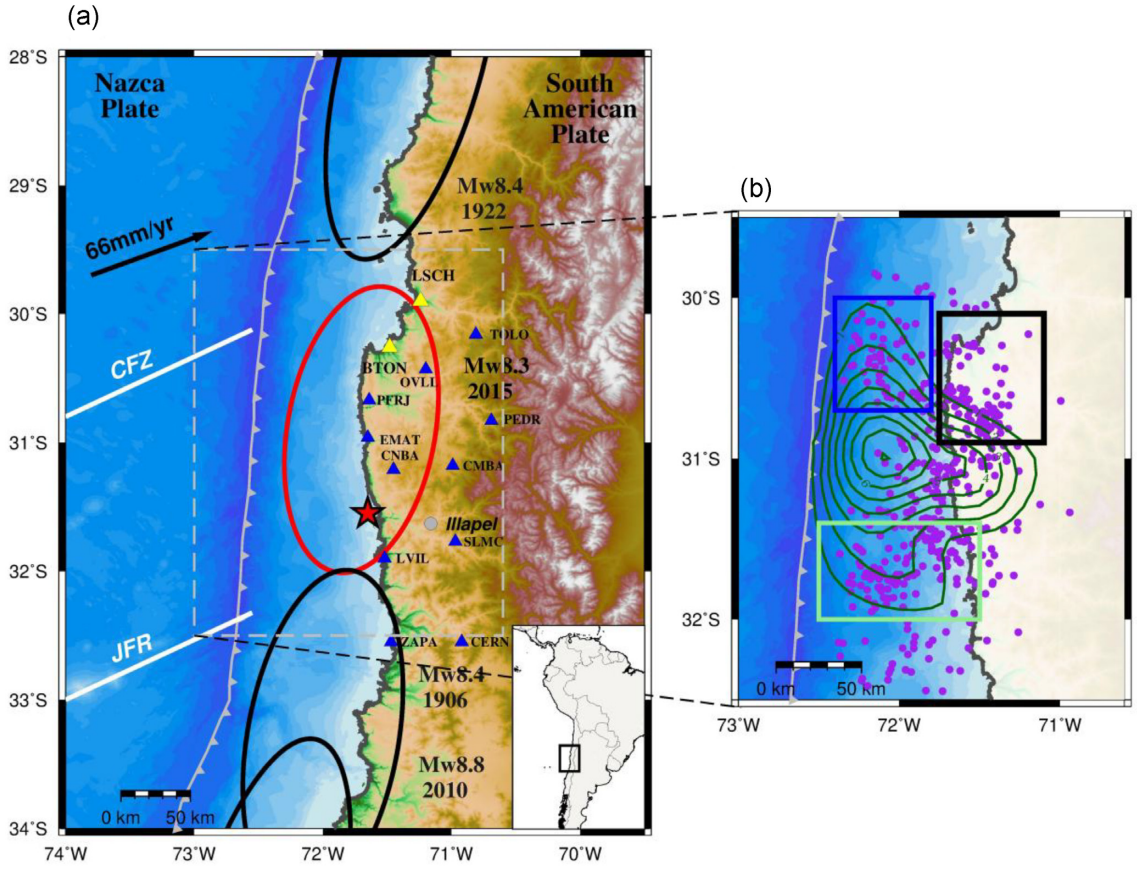

Figure 1. (a) Tectonic background of the 2015 Illapel earthquake. Black ellipses and red ellipse refer to the distribution of the rupture zone of the great historic earthquakes since 1900 and the Illapel earthquake, respectively (Vigny *et al.* 2011). Blue triangles represent the GPS sites and yellow triangles represent the GPS sites where liquefaction was observed (Gregory *et al.* 2015; Candia *et al.* 2017). Red star indicates the epicentre of the Illapel earthquake. The grey dot indicates the Illapel city. The black arrow indicates the convergence rate of the Nazca Plate against the South American Plate. The white bands are the Juan Fernandez Ridge (JFR) and the Challenger Fracture Zone (CFZ). The lower right illustration shows the location of the study region in the South American Plate. (b) The green contour shows the co-seismic slip distribution from Shrivastava *et al.* (2016). The purple dots represent the distribution of aftershocks (M_w > 4.5) within the first 2 yr following the Illapel event from the USGS catalogue (www.earthquake.usgs.gov). The blue, black and green boxes are the three areas with high pore fluid pressure delineated by Poli *et al.* (2017).

Darcy conductivity; and Q^{-1} represents the bulk compressibility. In practice, it is commodious to express parameters α, χ, Q^{-1} by the drained and undrained Poisson's ratio (v and v_u) and the Skempton parameter B (Skempton 1954; Rice & Cleary 1976):

$$\alpha = \frac{3(v_u - v)}{(1-2v)(1+v_u)B} \tag{5}$$

$$\chi = \frac{9}{2}\frac{(1-v_u)(v_u-v)D}{(1-v)(1+v_u)^2\mu B^2} \tag{6}$$

$$Q^{-1} = \frac{9}{2}\frac{(1-2v_u)(v_u-v)}{(1-2v)(1+v_u)^2\mu B^2} \tag{7}$$

where D is the hydraulic diffusivity. The overview on poroelastic parameters could refer to the studies of Kumpel (1991) and Wang (2000). Solving eqs (3) and (4), we could obtain the time-dependent displacements due to poroelastic rebound. Then we use the residual displacements (observed minus poroelastic relaxation) to invert for afterslip of the combined model (referred to here as residual afterslip) using the same strategies as above.

3 MODEL CONFIGURATION

For the pure afterslip model, we construct a seismogenic fault geometry with a dip of 19° and strike of N6°E, similar to previous studies (Shrivastava *et al.* 2016; Guo *et al.* 2019a). It has a spatial scale of approximately 300 km × 150 km, and is divided into 527 subfaults with a grid size of 10 km × 10 km. In addition, the rake angle is constrained within the range of 0°∼180°, and the maximum slip is set as 1 m. During the inversion, the horizontal and vertical displacements have the same weight, and the smoothing factor β is set as 0.25 based on the trade-off curve (Supporting Information Fig. S1). Green's functions are calculated based on a layered velocity model (Supporting Information Fig. S2).

During the poroelastic forward simulation of the combined model, the co-seismic slip model obtained by Shrivastava *et al.* (2016) is used as the driving model. Since the transient poroelastic effects are mainly controlled by the shallow geological structure, underground properties below 5 km have little impact on the poroelastic effects (Fielding *et al.* 2009; Nespoli *et al.* 2018; Wang *et al.* 2019). To improve the simulation resolution, we thus divide the crust above 5 km into three layers. Each layer considers a set of typical hydrologic parameters including the Skempton coefficient

B, Biot-Willis parameter α and hydraulic diffusivity D (e.g. Ingebritsen & Manning 2010; Kuang & Jiao 2014; Farías & Basualto 2020).

Because of the typical lack of sufficient observational constraints for hydrogeological conditions in the subduction zone, the model parameter space would be explored ideally with analyses of all possible combinations in reasonable ranges. The Biot-Willis parameter α is allowed to decrease from 0.9 to 0.3 with depth, reflecting its reduction with confining pressure (Wang 1993). For the Skempton coefficient B, a first-order assumption is $B = 1$ in many studies, considering fully saturated rocks in the entire domain and obtaining the maximum limit of the poroelastic effects. It is noted that some rocks may have $B < 1$ even if they are fully saturated (Makhnenko & Labuz 2013). Skempton (1954) voted that the value Bincreases with saturation, depending on the dryness of the surface and the deep fluid presence. In our model, B increases with depth, and the change is mainly concentrated in the shallow crust. In addition, the hydraulic diffusivity D shows a rapid decay with depth, consistent with the theoretical model (e.g. Ingebritsen & Manning 2010; Kuang & Jiao 2014). The number of parameters combined with the run time of each layer is beyond our computing power, we thus consider a set of model parameters typical of previous post-seismic studies for each layer (e.g. Nespoli *et al.* 2018; McCormack *et al.* 2020).

After we obtain the poroelastic displacements, we subtract them from the GPS data. Then, we use the residual displacements to invert the residual afterslip based on the same fault geometry and model space as the pure afterslip model. Here we utilize a guided trial and error approach, and systematically march through a range of each model parameter (α, B and D) to arrive at an initial combination that provides the minimum misfit (Fig. 2). Misfit is derived based on the root mean square of all horizontal and vertical GPS displacements. In the fine-tuning stage, we not only find the optimal value for each model parameter, but also get the best-fitting, depth-dependent structure. The optimal model parameters are shown in Supporting Information Table S1. Compared with the pure afterslip model, the combined model with a three-layered shallow crust has a smaller error and is more physically reasonable, which is considered our preferred model (Supporting Information Table S2).

4 RESULTS

4.1 Pure afterslip distribution

Fig. 3(a) illustrates our optimal pure afterslip distribution, and Fig. 3(b) shows the comparison between GPS observations and predictions. Model results show that the peak slip is 0.51 m, similar to the results of Shrivastava *et al.* (2016) (0.50 m) and Barnhart *et al.* (2016) (0.52 m). The seismic moment is 2.6×10^{20} N m, equivalent to an M_w 7.54 event, consistent with the results of Barnhart *et al.* (2016). Similar to previous studies (Barnhart *et al.* 2016; Shrivastava *et al.* 2016; Guo *et al.* 2019a), there are two asperities distributed on the north and south sides of the co-seismic high-slip region. These two patches begin to form about 10 d after the Illapel earthquake (Shrivastava *et al.* 2016; Guo *et al.* 2019a). By 1.5 months after this event, the maximum slip reaches ∼0.5 m at a depth of 20–40 km. In contrast, the northern large slip patch is shallower than the southern one. Through the pure afterslip model, the first-order simulation of the transient post-seismic deformation can be obtained (Wang *et al.* 2019). However, for some GPS stations, there are significant differences between observations and predictions in the horizontal (OVLL, TOLO, PEDR) and vertical (CNBA, CMBA, SLMC) components, which is hard to explain in the pure afterslip model.

4.2 Residual afterslip and poroelastic deformation

Fig. 4(a) shows the residual afterslip distribution, which is still composed of two large slip patches. So considering the poroelasticity does not change the basic afterslip pattern for the Illapel earthquake. However, the slip scope and magnitude in the northern asperity are significantly shrunk, and the southern asperity becomes larger (Fig. 4a). The peak afterslip of the combined model is 0.71 m, remarkably different from the pure afterslip model. Therefore, the crust deformation produced by poroelastic rebound may be misinterpreted as afterslip. Differencing the pure afterslip and residual afterslip generates the surface deformation due to poroelasticity, as shown in Fig. 4(b). Therefore, we propose that the pure afterslip model overestimates the afterslip of the northern and southern segments and underestimates the middle slip (Fig. 4b), with local errors of up to 50 per cent or more (Fig. 4c). In addition, we find that the co-seismic high-slip region, afterslip, and poroelastic effects present a complementary pattern, even if there is a partial overlap (Fig. 4b). Afterslip and high pore pressure areas together constitute a velocity-strengthening region, hindering the co-seismic rupture.

A comparison of all displacements for the assumed poroelastic structure (Supporting Information Table S1) and inferred residual afterslip is demonstrated in Figs 5(a) and (b), respectively. Predicted displacements associated with the combined afterslip and poroelastic relaxation models are compared to the observed displacements in Fig. 5(c). The combined model could explain all observed horizontal and vertical displacements satisfactorily. Results show that poroelastic effects have a significant influence on the early post-seismic process, especially for the vertical displacements, and the local deformation could reach the magnitude of centimetres (Fig. 5a). Most vertical poroelastic displacements appear to be opposite in sense to the co-seismic vertical deformation (Fig. 5a, Supporting Information Fig. S3). The horizontal poroelastic deformation is lower than the vertical deformation (Fig. 5a), as it does not depend on the regional fluid enrichment degree, but on the change of fluid gradient (Albano *et al.* 2017; Nespoli *et al.* 2018; McCormack *et al.* 2020). Similar phenomena have been observed in previous studies (e.g. Peltzer *et al.* 1996; Jonsson *et al.* 2003).

5 DISCUSSION

Our preferred model reveals the concurrent occurrence of poroelastic relaxation and afterslip within the first 1.5 months after the 2015 M_w 8.3 Illapel earthquake. At this time, the question of what is the timescale of total poroelastic rebound arises, which is of great significance to improve the understanding of post-seismic mechanisms and infer the continued aseismic slip on the fault plane. In general, timescales of days to months are associated with the poroelastic rebound (Jonsson *et al.* 2003; Fialko 2004; Hetland & Hager 2006), which could be defined as $t = L^2/D$, where L represents the characteristic distance for fluid diffusion and Ddenotes the hydraulic diffusivity as mentioned earlier. In the shallowest crust, given that L is of the order of 10 km (e.g. McCormack & Hesse 2018; Fialko *et al.* 2021) and the optimal hydraulic diffusivity is $8\ m^2\ s^{-1}$ (Fig. 2), t is estimated to be larger than ∼140 d. A longer diffusion distance would imply a larger value of diffusive relaxation timescale. Therefore, poroelasticity plays a non-negligible role for a

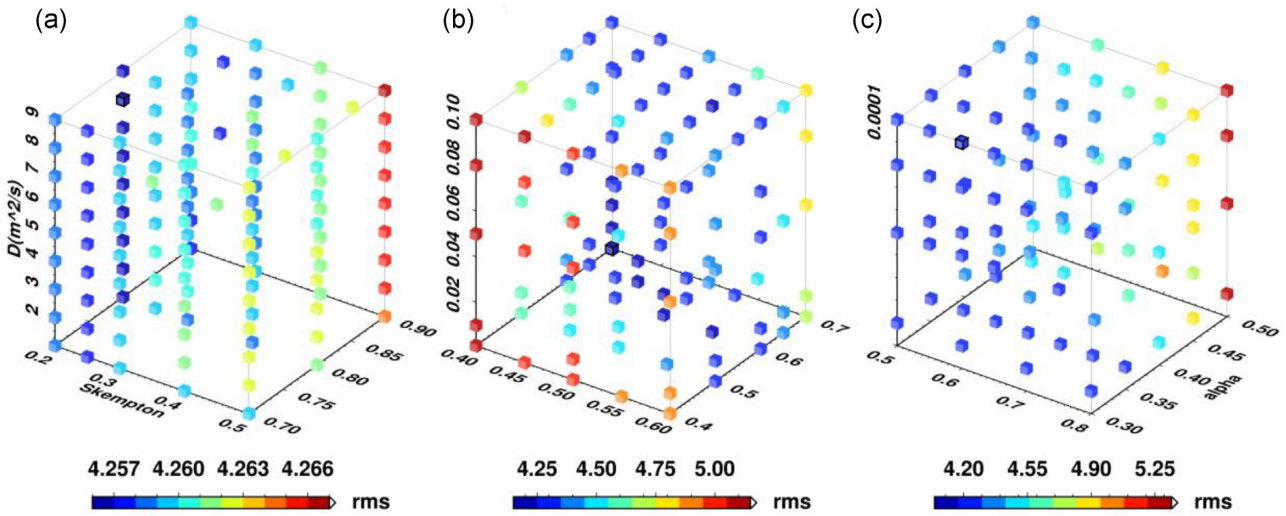

Figure 2. Misfits of test models considering variations in the pore parameters B, α and D for (a) the first layer (0–0.19 km), (b) the second layer (0.19–2.5 km) and (c) the third layer (2.5–5.32 km). The black line cube is the optimal model for each layer.

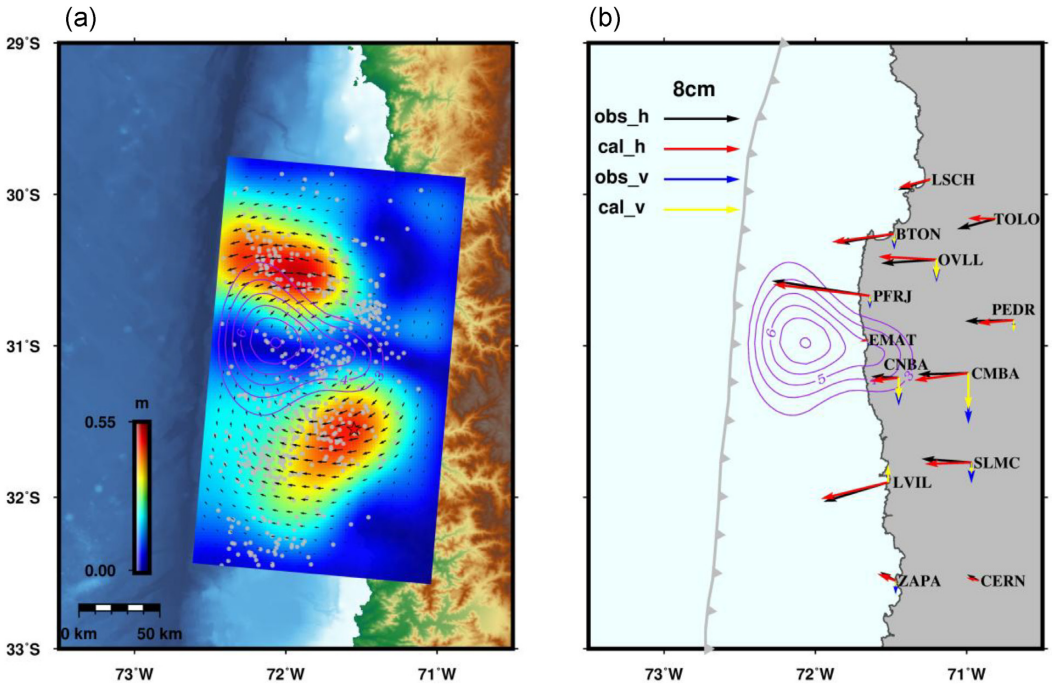

Figure 3. Afterslip distribution and data fitting from the optimal pure afterslip model. (a) Afterslip distribution. Red star is the epicentre of the 2015 Illapel event. Grey dots are the aftershocks ($M_w > 4.5$) within 1.5 months after the earthquake from the USGS catalogue (www.earthquake.usgs.gov). Black arrows show the slip direction. (b) Comparison of observed and calculated displacements. The purple contour is the co-seismic slip from Shrivastava *et al.* (2016) (slip > 3 m).

long time after the 2015 Illapel earthquake. In addition, the vertical diffusivity variation effectively creates a layered structure, which may lead to multiple poroelastic relaxation timescales and more complicated poroelastic responses (McCormack *et al.* 2020).

The geological conditions of different regions may vary a lot, so the poroelastic effects have different responses in different seismic events. Compared with the viscoelastic relaxation related to the deep structure, the poroelastic effects may be more variable and irregular. Poroelastic components of the 2012 M_w 7.6 Nicoya earthquake are distributed in a patch 25–90 km away from the trench (McCormack *et al.* 2020), overlapping most of the co-seismic high-slip areas (Yue *et al.* 2013). For the 2011 M_w 9.0 Tohoku earthquake, poroelastic rebound produces surface displacements mostly in a narrow zone close to the trench in the oceanic crust while producing displacements across a broader zone in the continental upper plate (Hu *et al.* 2014). As for the Illapel earthquake, the post-seismic slip caused by poroelastic effects is mainly concentrated on the north and south sides of the co-seismic rupture area.

Finally, there are still some limitations in the simulation of poroelastic effects. The GPS observations used here are less sensitive to slip at depth, which may lead to larger uncertainties in deeper slip. The assumption of linear poroelasticity means that the model cannot

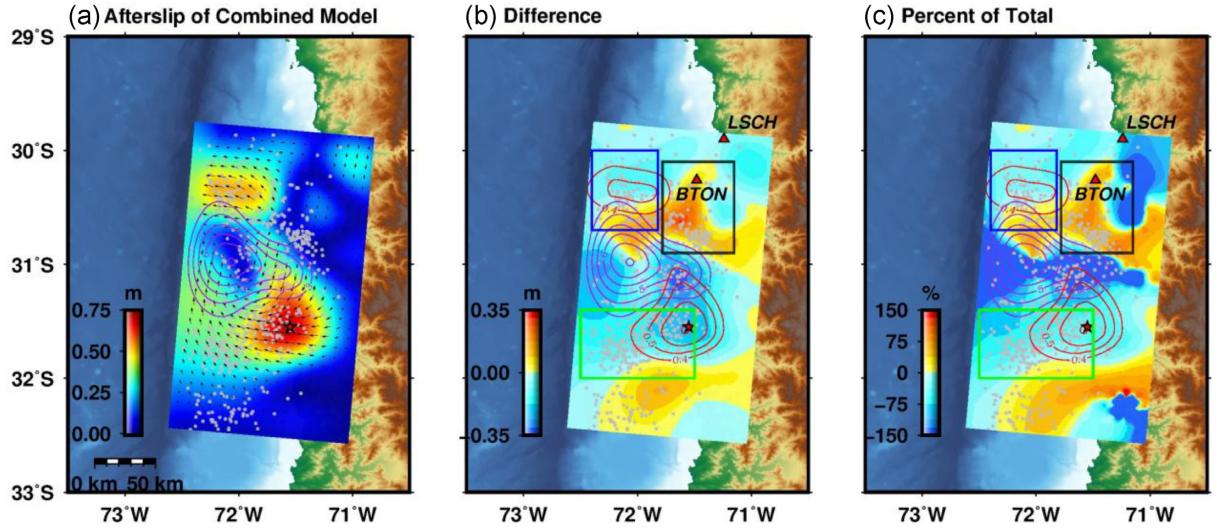

Figure 4. Afterslip differences assuming both with and without poroelastic effects. (a) Afterslip distribution from the combined model involving the poroelastic effects. (b) Afterslip differences between the pure afterslip model and the combined model (pure afterslip model minus combined model). (c) Per cent of the afterslip component that can accounted for by poroelasticity (afterslip differences divided by pure afterslip). Positive (red) regions indicate where afterslip is overestimated while negative (blue) regions represent where afterslip is underestimated. The red line is the afterslip contour with slip >0.4 m based on our preferred combined model. Red triangles represent the GPS stations with observable liquefaction phenomenon. The blue, black and green rectangles are the regions with high pore pressure delineated by Poli *et al.* (2017). Other symbols are the same as Fig. 3.

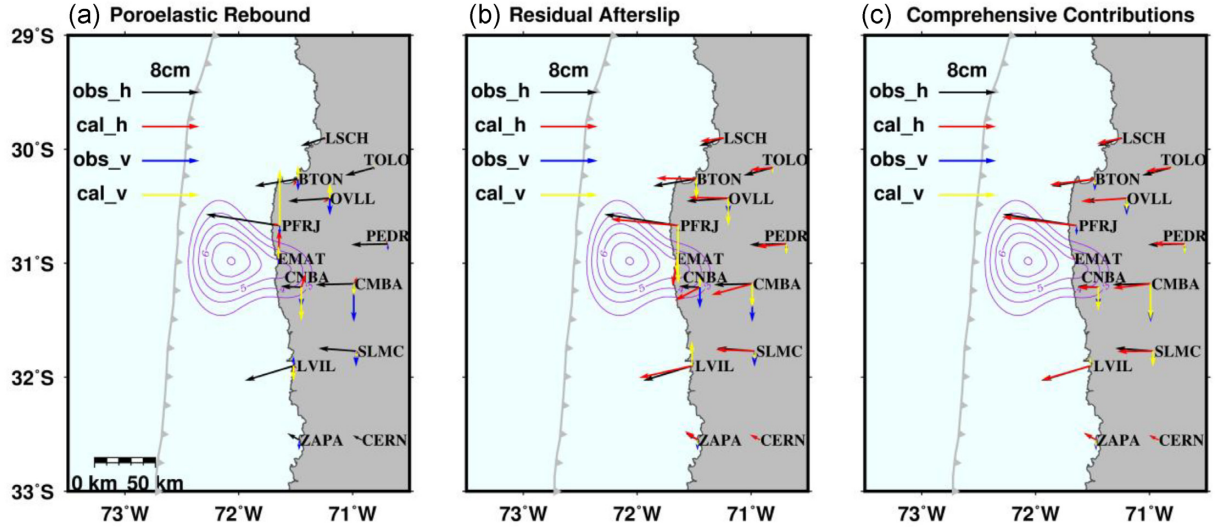

Figure 5. Comparison of observed and calculated displacements based on (a) the poroelastic rebound, (b) the residual afterslip and (c) their comprehensive contributions. Other symbols are the same as Fig. 3.

consider the influence of dynamic stress changes nor the consolidation processes occurring during and after the earthquake. For the early post-seismic phase, the poroelastic effects are mainly related to the shallow crust structure rich in loose sediment, where the consolidation process may affect the pore pressure response to the earthquake (Fielding *et al.* 2009; Nespoli *et al.* 2018; Wang *et al.* 2019). In addition, earthquakes themselves can even cause a single order of magnitude change in the permeability of near-surface areas (Rojstaczer *et al.* 1995; Manga *et al.* 2012), and fractures generally increase permeability below the shallow crust, reducing the time for poroelastic relaxation. Moreover, subduction zone earthquakes could cause pressure on coastal areas and discharge large amounts of pore water through the seafloor, commonly known as subsea groundwater exchange (McCormack & Hesse 2018), which is also ignored here. These all put forward higher requirements on the model and data accuracy. Besides that, Guo *et al.* (2019a) suggested that the pure afterslip model ignoring the viscoelastic relaxation underestimated afterslip updip and overestimated afterslip downdip of the rupture zone. Therefore, although our results indicate that the poroelastic effects have significant contributions to the transient post-seismic deformation, it should be more reasonable to consider the influence of poroelastic rebound, afterslip and viscoelastic relaxation simultaneously, which may further improve our understanding of post-seismic mechanisms after large earthquakes (King *et al.* 1994; Tung & Masterlark 2018; Tung *et al.* 2018; Albano *et al.* 2019).

Even so, the influence of limitations from different sources on our model is mainly transformed into the variability of poroelastic

parameters. Regarding the typical values of poroelastic coefficients α, B and D, we test the reliability of our result with the variation of parameters over multiple ranges and scales (Fig. 2), and the root-mean-square misfits of combined models are always better than that of the pure afterslip model, confirming that the variability of parameters would not significantly change our conclusions of poroelastic effects associated with the post-seismic deformation. We thus argue that poroelasticity indeed plays an important role in the early post-seismic deformation and our result is robust.

6 CONCLUSIONS

In this paper, we use the cGPS observations within the first 1.5 months after the 2015 M_w 8.3 Illapel earthquake to study the influence of poroelastic effects on the early post-seismic deformation. Model results show the widespread distribution of fluid flow in seismic fault areas and the significant influence of poroelastic rebound on the early post-seismic process. Previous pure afterslip models introduce errors of ∼20 and >50 per cent locally. Therefore, the poroelastic effects with regional characteristics cannot be ignored in the transient post-seismic deformation, which can either amplify or mute post-seismic signals.

ACKNOWLEDGMENTS

We thank the editor Kosuke Heki, assistant editor Fern Storey and three anonymous reviewers for comments that improved this manuscript. This research is supported by grants from B-type Strategic Priority Program of the Chinese Academy of Sciences (No. XDB41000000), National Natural Science Foundation of China (NSFC; No. 41874026) and the Key Research Program of the Chinese Academy of Sciences (No. KFZD-SW-428). RG designed research; Haozhe Yang performed research and wrote the paper; Hongfeng Yang contributed to supervision and validation; JZ and HS provided theoretical and methodological guidance.

DATA AVAILABILITY

The cGPS observations used in this work are from the open data of Shrivastava *et al.* (2016). We apply the program PEGRN/PECMP to simulate the effects of poroelastic rebound and invoke the code SDM to invert the residual afterslip distribution, which are available from ftp://ftp.gfz-potsdam.de/pub/home/turk/wang.

REFERENCES

Albano, M., Barba, S., Saroli, M., Polcari, M., Bignami, C., Moro, M., Stramondo, S. & Di Bucci, D., 2019. Aftershock rate and pore fluid diffusion: insights from the Amatrice–Visso–Norcia (Italy) 2016 seismic sequence, *J. geophys. Res.,* **124**(1), 995–1015.

Albano, M., Barba, S., Solaro, G., Pepe, A., Bignami, C., Moro, M., Saroli, M. & Stramondo, S., 2017. Aftershocks, groundwater changes and post-seismic ground displacements related to pore pressure gradients: insights from the 2012 Emilia–Romagna earthquake, *J. geophys. Res.,* **122**(7), 5622–5638.

Angermann, D., Klotz, J. & Reigber, C., 1999. Space-geodetic estimation of the Nazca–South America Euler vector, *Earth planet. Sci. Lett.,* **171**(3), 329–334.

Barbot, S., Fialko, Y. & Bock, Y., 2009. Postseismic deformation due to the M_w6.0 2004 Parkfield earthquake: stress-driven creep on a fault with spatially variable rate-and-state friction parameters, *J. geophys. Res.,* **114**(B7), https://dx.doi.org/10.1029/2008jb005748.

Barnhart, W.D., Murray, J.R., Briggs, R.W., Gomez, F., Miles, C.P.J., Svarc, J., Riquelme, S. & Stressler, B.J., 2016. Coseismic slip and early afterslip of the 2015 Illapel, Chile, earthquake: implications for frictional heterogeneity and coastal uplift, *J. geophys. Res.,* **121**(8), 6172–6191.

Biot, M.A., 1941. General theory of three-dimensional consolidation, *J. Appl. Phys.,* **12**(2), 155–164.

Bouchon, M., 1997. The state of stress on some faults of the San Andreas System as inferred from near-field strong motion data, *J. geophys. Res.,* **102**(B6), 11 731–11 744.

Bürgmann, R. & Dresen, G., 2008. Rheology of the lower crust and upper mantle: evidence from rock mechanics, geodesy, and field observations, *Annu. Rev. Earth Planet. Sci.,* **36**(1), 531–567.

Candia, G., de Pascale, G.P., Montalva, G. & Ledezma, C., 2017. Geotechnical aspects of the 2015 M_w 8.3 Illapel megathrust earthquake sequence in Chile, *Earthq. Spectra,* **33**(2), 709–728.

Cheng, A.H.-D., 2016. *Poroelasticity,* Springer International Publishing.

Farías, C. & Basualto, D., 2020. Reactivating and calming volcanoes: the 2015M_w 8.3 Illapel megathrust strike, *Geophys. Res. Lett.,* **47**(16), https://dx.doi.org/10.1029/2020gl087738.

Fialko, Y., 2004. Evidence of fluid-filled upper crust from observations of postseismic deformation due to the 1992 M_w7.3 Landers earthquake, *J. geophys. Res.,* **109**(B8), https://dx.doi.org/10.1029/2004jb002985.

Fialko, Y., Jin, Z., Zubovich, A. & Schöne, T., 2021. Lithospheric deformation due to the 2015 M7.2 Sarez (Pamir) earthquake constrained by 5 years of space geodetic observations, *Earth Space Sci. Open Arch.,* **49,** https://dx.doi.org/doi:10.1002/essoar.10508106.1.

Fielding, E.J., Lundgren, P.R., Burgmann, R. & Funning, G.J., 2009. Shallow fault-zone dilatancy recovery after the 2003 Bam earthquake in Iran, *Nature,* **458**(7234), 64–68.

Freed, A.M., Hashima, A., Becker, T.W., Okaya, D.A., Sato, H. & Hatanaka, Y., 2017. Resolving depth-dependent subduction zone viscosity and afterslip from postseismic displacements following the 2011 Tohoku-oki, Japan earthquake, *Earth planet. Sci. Lett.,* **459,** 279–290.

Freed, A.M. & Lin, J., 2001. Delayed triggering of the 1999 Hector Mine earthquake by viscoelastic stress transfer, *Nature,* **411**(6834), 180–183.

Gregory P., De Pascale, Montalva, G., Candia, G. & Ledezma, C., 2015. Geotechnical reconnaissance of the 2015 M_w8.3 Illapel, Chile earthquake.

Guo, R., Zheng, Y., Xu, J. & Jiang, Z., 2019b. Seismic and aseismic fault slip associated with the 2017 M_w 8.2 Chiapas, Mexico, earthquake sequence, *Seismol. Res. Lett.,* **90**(3), 1111–1120.

Guo, R., Zheng, Y., Xu, J. & Riaz, M.S., 2019a. Transient viscosity and afterslip of the 2015 M_w 8.3 Illapel, Chile, earthquake, *Bull. seism. Soc. Am.,* **109**(6), 2567–2581.

Helmstetter, A. & Shaw, B.E., 2009. Afterslip and aftershocks in the rate-and-state friction law, *J. geophys. Res.,* **114**(B1), https://dx.doi.org/10.1029/2007jb005077

Hetland, E.A. & Hager, B.H., 2006. The effects of rheological layering on post-seismic deformation, *Geophys. J. Int.,* **166**(1), 277–292.

Hu, Y., Burgmann, R., Freymueller, J.T., Banerjee, P. & Wang, K.L., 2014. Contributions of poroelastic rebound and a weak volcanic arc to the postseismic deformation of the 2011 Tohoku earthquake, *Earth Planets Space,* **66,** https://dx.doi.org/Artn 10610.1186/1880-5981-66-106

Huang, H., Xu, W., Meng, L., Bürgmann, R. & Baez, J.C., 2017. Early aftershocks and afterslip surrounding the 2015 Mw 8.4 Illapel rupture, *Earth planet. Sci. Lett.,* **457,** 282–291.

Ingebritsen, S.E. & Manning, C.E., 2010. Permeability of the continental crust: dynamic variations inferred from seismicity and metamorphism, *Geofluids,* **10,** 193–205.

Jonsson, S., Segall, P., Pedersen, R. & Bjornsson, G., 2003. Post-earthquake ground movements correlated to pore-pressure transients, *Nature,* **424**(6945), 179–183.

King, G., Stein, R. & Lin, J., 1994. Static stress changes and the triggering of earthquakes, *Bull. seism. Soc. Am.,* **84,** 935–953.

Klein, E., Vigny, C., Fleitout, L., Grandin, R., Jolivet, R., Rivera, E. & Métois, M., 2017. A comprehensive analysis of the Illapel 2015 M_w8.3 earthquake from GPS and InSAR data, *Earth planet. Sci. Lett.,* **469,** 123–134.

Kuang, X. & Jiao, J.J., 2014. An integrated permeability-depth model for Earth's crust, *Geophys. Res. Lett.,* **41**(21), 7539–7545.
Kumpel, H.-J., 1991. Poroelasticity: parameters reviewed, *Geophys. J. Int.,* **105**(3), 783–799
Makhnenko, R. & Labuz, J., 2013. Saturation of porous rock and measurement of B coefficient, https://dx.doi.org/10.13140/RG.2.1.1373.3604
Malservisi, R. *et al.*, 2015. Multiscale postseismic behavior on a megathrust: the 2012 Nicoya earthquake, Costa Rica, *Geochem. Geophys. Geosyst.,* **16**(6), 1848–1864.
Manga, M., Beresnev, I., Brodsky, E.E., Elkhoury, J.E., Elsworth, D., Ingebritsen, S.E., Mays, D.C. & Wang, C.-Y., 2012. Changes in permeability caused by transient stresses: field observations, experiments, and mechanisms, *Rev. Geophys.,* **50**(2),. https://dx.doi.org/10.1029/2011rg000382
Marone, C.J., Scholtz, C.H. & Bilham, R., 1991. On the mechanics of earthquake afterslip, *J. geophys. Res.,* **96**(B5), https://dx.doi.org/10.1029/91jb00275
McCormack, K., Hesse, M.A., Dixon, T. & Malservisi, R., 2020. Modeling the contribution of poroelastic deformation to postseismic geodetic signals, *Geophys. Res. Lett.,* **47**(8), https://dx.doi.org/10.1029/2020gl086945
McCormack, K.A. & Hesse, M.A., 2018. Modeling the poroelastic response to megathrust earthquakes: a look at the 2012 M 7.6 Costa Rican event, *Adv. Water Res.,* **114,** 236–248.
Nespoli, M., Belardinelli, M.E., Gualandi, A., Serpelloni, E. & Bonafede, M., 2018. Poroelasticity and fluid flow modeling for the 2012 Emilia–Romagna earthquakes: hints from GPS and InSAR data, *Geofluids,* **2018,** 1–15.
Peltzer, G., Rosen, P., Rogez, F. & Hudnut, K., 1996. Postseismic rebound in fault step-overs caused by pore fluid flow, *Science,* **273**(5279), 1202–1204.
Perfettini, H. & Avouac, J.P., 2004. Postseismic relaxation driven by brittle creep: a possible mechanism to reconcile geodetic measurements and the decay rate of aftershocks, application to the Chi-Chi earthquake, Taiwan, *J. geophys. Res.,* **109**(B2), https://dx.doi.org/10.1029/2003jb002488
Poli, P., Jeria, A.M. & Ruiz, S., 2017. The M_w8.3 Illapel earthquake (Chile): preseismic and postseismic activity associated with hydrated slab structures, *Geology,* **45**(3), 247–250.
Rice, J.R. & Cleary, M.P., 1976. Some basic stress diffusion solutions for fluid-saturated elastic porous-media with compressible constituents, *Rev. Geophys.,* **14**(2), 227–241.
Roeloffs, E., 1996. Poroelastic techniques in the study of earthquake-related hydrologic phenomena, *Adv. Geophys.,* **37,** 135–195.
Rojstaczer, S., Wolf, S. & Michel, R., 1995. Permeability enhancement in the shallow crust as a cause of earthquake-induced hydrological changes, *Nature,* **373**(6511), 237–239.
Shrivastava, M.N. *et al.*, 2016. Coseismic slip and afterslip of the 2015 M_w 8.3 Illapel (Chile) earthquake determined from continuous GPS data, *Geophys. Res. Lett.,* **43**(20), 10 710–10 719.
Skempton, A.W., 1954. The pore-pressure coefficients A and B, *Géotechnique,* **4**(4), 143–147
Tang, X., Guo, R., Xu, J., Sun, H., Chen, X. & Zhou, J., 2021. Probing the fault complexity of the 2017 Ms 7.0 Jiuzhaigou earthquake based on the InSAR data, *Remote Sens.,* **13**(8), 1573. https://doi.org/10.3390/rs13081573
Tilmann, F. *et al.*, 2016. The 2015 Illapel earthquake, central Chile: a type case for a characteristic earthquake?, *Geophys. Res. Lett.,* **43**(2), 574–583.
Tung, S. & Masterlark, T., 2018. Delayed poroelastic triggering of the 2016 October Visso earthquake by the August Amatrice earthquake, Italy, *Geophys. Res. Lett.,* **45**(5), 2221–2229.
Tung, S., Masterlark, T. & Dovovan, T., 2018. Transient poroelastic stress coupling between the 2015 M7.8 Gorkha, Nepal earthquake and its M7.3 aftershock, *Tectonophysics,* **733,** 119–131.
Vigny, C. *et al.*, 2011. The 2010 M_w 8.8 Maule megathrust earthquake of Central Chile, monitored by GPS, *Science,* **332**(6036), 1417–1421.
Wang, H.F., 1993. Quasi-static poroelastic parameters in rock and their geophysical applications, *Pure appl. Geophys.,* **141**(2–4), 269–286.
Wang, H.F., 2000. *Theory of Linear Poroelasticity,* Princeton University Press.
Wang, L., Wang, R., Roth, F., Enescu, B., Hainzl, S. & Ergintav, S., 2009. Afterslip and viscoelastic relaxation following the 1999 *M* 7.4 İzmit earthquake from GPS measurements, *Geophys. J. Int.,* **178**(3), 1220–1237.
Wang, R.J. & Kumpel, H.J., 2003. Poroelasticity: efficient modeling of strongly coupled, slow deformation processes in a multilayered half-space, *Geophysics,* **68**(2), 705–717.
Wang, S., Xu, W., Xu, C., Yin, Z., Bürgmann, R., Liu, L. & Jiang, G., 2019. Changes in groundwater level possibly encourage shallow earthquakes in Central Australia: the 2016 Petermann Ranges earthquake, *Geophys. Res. Lett.,* **46**(6), 3189–3198.
Yin, J., Yang, H., Yao, H. & Weng, H., 2016. Coseismic radiation and stress drop during the 2015 M_w8.3 Illapel, Chile megathrust earthquake, *Geophys. Res. Lett.,* **43,** 1520–1528.
Yue, H., Lay, T., Schwartz, S.Y., Rivera, L., Protti, M., Dixon, T.H., Owen, S. & Newman, A.V., 2013. The 5 September 2012 Nicoya, Costa Rica M_w7.6 earthquake rupture process from joint inversion of high-rate GPS, strong-motion, and teleseismic *P* wave data and its relationship to adjacent plate boundary interface properties, *J. geophys. Res.,* **118**(10), 5453–5466.

SUPPORTING INFORMATION

Supplementary data are available at *GJI* online.

Figure S1. Trade-off curves between the model roughness and data misfit. (a) Trade-off curve for the pure afterslip model and (b) the combined model. In both cases, 0.25 is selected as the optimal smoothing factor.
Figure S2. Layered velocity model used in this work.
Figure S3. GPS observations for (a) co-seismic offsets and (b) cumulative post-seismic displacements within 1.5 months of the 2015 Illapel earthquake.
Table S1. Table of the chosen optimal parameter values for the model.
Table S2. Description and misfit of sample models.

Please note: Oxford University Press is not responsible for the content or functionality of any supporting materials supplied by the authors. Any queries (other than missing material) should be directed to the corresponding author for the paper.